PROCEEDINGS OF SPIE

SPIEDigitalLibrary.org/conference-proceedings-of-spie

MAVIS Adaptive Optics Module: optical configuration and expected performance

Davide Greggio, Brian Taylor, Marco Bonaglia, Valentina Viotto, Maria Bergomi, et al.

Davide Greggio, Brian Taylor, Marco Bonaglia, Valentina Viotto, Maria Bergomi, Enrico Pinna, Guido Agapito, Stefan Ströbele, Matteo Aliverti, Kalyan Radhakrishnan, Christian Schwab, Jesse Cranney, Israel Vaughn, Luca Marafatto, Demetrio Magrin, David Brodrick, Simonetta Chinellato, François Rigaut, "MAVIS Adaptive Optics Module: optical configuration and expected performance," Proc. SPIE 12185, Adaptive Optics Systems VIII, 121856P (29 August 2022); doi: 10.1117/12.2630017

Event: SPIE Astronomical Telescopes + Instrumentation, 2022, Montréal, Québec, Canada

SPIE.

Downloaded From: https://www.spiedigitallibrary.org/conference-proceedings-of-spie on 27 Nov 2023 Terms of Use: https://www.spiedigitallibrary.org/terms-of-use

MAVIS Adaptive Optics Module: optical configuration and expected performance

Davide Greggio[a], Brian Taylor[b], Marco Bonaglia[c], Valentina Viotto[a], Maria Bergomi[a], Enrico Pinna[c], Guido Agapito[c], Stefan Ströbele[d], Matteo Aliverti[e], Kalyan Radhakrishnan[a], Christian Schwab[f], Jesse Cranney[b], Israel Vaughn[b], Luca Marafatto[a], Demetrio Magrin[a], David Brodrick[b], Simonetta Chinellato[a], and François Rigaut[b]

[a]INAF - Osservatorio Astronomico di Padova (Italy)
[b]The Australian National Univ. (Australia)
[c]INAF - Osservatorio Astrofisico di Arcetri (Italy)
[d]European Southern Observatory (Germany)
[e]INAF - Osservatorio Astronomico di Brera (Italy)
[f]Macquarie Univ. (Australia)

ABSTRACT

The MCAO Assisted Visible Imager and Spectrograph (MAVIS) is currently in preliminary design for the ESO VLT. The instrument will provide multi-conjugate adaptive optics correction over a wide field of 30"x30", feeding the visible part of the spectrum (from 370 to 1000nm) to an imager and a spectrograph. The Adaptive Optics Module (AOM) of MAVIS implements two deformable mirrors, composed by more than 2000 actuators each, and includes a Laser Guide Star (LGS) and a Natural Guide Star (NGS) wavefront sensor for the tomographic reconstruction and correction of the atmospheric turbulence. Moreover, it provides other key functionalities like atmospheric dispersion compensation and field de-rotation, delivering a corrected diffraction-limited 30"x30" focal plane to three output ports: one for the imager, one for the spectrograph and one for visiting instruments. In this paper we describe the current optical configuration of the AOM, and we report the results of the analyses conducted to evaluate the expected optical performance of the system. The analyses include simulations for the manufacturing and alignment tolerances, sensitivity to mid-spatial frequency figure errors and their impact to astrometry.

Keywords: Adaptive Optics, Multi-Conjugate Adaptive Optics, MCAO, optical design, optical performance, astrometric error

1. INTRODUCTION

MAVIS is an instrument conceived for imaging and spectroscopic observations in the visible waveband,[1] taking advantage of the high spatial resolution obtained with adaptive optics correction at an 8-m class telescope ($\lambda/D = 14mas$ @ $550nm$ for the VLT). The instrument implements the Multi-Conjugate Adaptive Optics (MCAO) technique[2] to obtain wavefront correction over a wide field of $30 \times 30 arcsec$. The wavefront sensing is done with eight sodium Laser Guide Stars (LGSs),[3] launched from the VLT UT4, and up to three Natural Guide Stars (NGSs) selectable over a technical field of $2 arcmin$ diameter. The wavefront correction is done with the Deformable Secondary Mirror (DSM)[4] of the telescope in combination with two Alpao DMs placed inside MAVIS, each composed by more than 2000 actuators and conjugated at an altitude of 6km and 13.5km respectively.

To ease organization of work within the instrument consortium, MAVIS has been structured with modularity in mind and it is currently constituted by four main sub-systems which have a high level of independence one from the other:

Further author information: (Send correspondence to Davide Greggio)
Davide Greggio: E-mail: davide.greggio@inaf.it

Adaptive Optics Systems VIII, edited by Laura Schreiber, Dirk Schmidt, Elise Vernet,
Proc. of SPIE Vol. 12185, 121856P · © 2022 SPIE
0277-786X · doi: 10.1117/12.2630017

Downloaded From: https://www.spiedigitallibrary.org/conference-proceedings-of-spie on 27 Nov 2023
Terms of Use: https://www.spiedigitallibrary.org/terms-of-use

- **Adaptive Optics Module (AOM),**[5,6]: it is the sub-system providing wavefront sensing and correction capability and it is the subject of this paper. The AOM also includes an Atmospheric Dispersion Corrector (ADC) and an optical field de-rotator. The sub-system is divided in three main modules plus an additional channel used for engineering purposes:
    - **Post Focal Relay (PFR)**: it is the common-path optical relay that includes DMs, ADC and de-rotator. It splits the light with dichroic filters sending it to the wavefront sensors and to the instrument ports
    - **LGS Wavefront Sensor (LGS-WFS)**: it is the module providing high-order wavefront sensing using the light from the eight LGSs
    - **NGS Wavefront Sensor (NGS-WFS)**[7]: it is the module providing low-order (tip-tilt, astigmatism and focus) wavefront sensing using the light from up to three NGSs placed within the technical field.
    - **Diagnostic and NCPA Unit (DNU)**: it is a module used for engineering purposes. It provides WFS capabilities through a 40x40 Shack-Hartmann WFS and pupil imaging capabilities for on-axis sources.
- **Imager**:[8] the imaging camera that includes the science filter wheels and the cryogenic detector.
- **Spectrograph**:[8] it includes re-imaging optics, a field slicer and a collimator/camera system with a set of dispersing elements. The field is split in two channels.
- **Calibration Unit (CU)**: it includes the distortion grid for distortion calibration and a set of sources (point-like or diffuse) for the calibration of the instruments and of the AO system.

In the previous phases of the project, several optical solutions have been considered for the AOM, spanning a range from all-reflective, cata-dioptric and all refractive designs. In this paper, we describe the latest optical configuration proposed, which is the baseline for the PDR. Moreover, we report the nominal performances and we describe some of the analyses conducted to estimate the impact of manufacturing and alignment on the final performance of the system. The latter include the sensitivity and Monte Carlo tolerance analyses and the astrometric error induced by mid-high spatial frequency distortions.

2. OPTICAL DESIGN

The optical configuration of the AOM is the result of a set of trade-off studies[9] and designs. It is based on an all-refractive, on-axis approach, meaning that the are no mirrors or off-axis optical elements with power. The main advantages of this choice are: 1) a very good correction of distortion and optical aberrations both for infinite-conjugate (NGSs, sky) and finite-conjugate (LGSs) objects without the need to use optical elements placed very close to the focal plane, 2) easier manufacturing of the optical components, and 3) easier alignment of the system. The main disadvantage is the need to correct for chromatic aberrations which, due to the very broad spectral range required (from 370nm to 1740nm), require the use of special low-dispersion glasses and complex AR coatings.

The optical layout is shown in the figure below. The F/15 beam coming from the telescope (left of Figure 1) is relayed by a field lens to two DMs: the first conjugated at 13.5km altitude and the second conjugated at 6km altitude. A cemented triplet then, collimates the infinity-conjugated beam, forming an image of the telescope pupil (Adaptive Secondary Mirror) of $\sim 58mm$ diameter. The pupil plane is accessible and a pupil stop can be inserted when the system is fed by the CU, to select the proper beam size. Just after the pupil plane, a dichroic filter reflects the LGS light (589nm wavelength) towards the LGS channel and transmits all the other wavelengths towards the ADC, constituted by two counter-rotating compound prisms.[10] After the ADC, a fairly big K-Mirror is used for field de-rotation of the full technical field. Finally the light is split by a second dichroic which reflects the visible light (370-1000nm) towards the Science channel objective and transmits the NIR light (1000-1740nm) towards the NGS channel objective.

In the LGS channel, a three-lens objective with two moving components can adjust the focus conjugation distance in the range 80-230km and is able to keep the LGS stars in focus at the output focal plane without

Downloaded From: https://www.spiedigitallibrary.org/conference-proceedings-of-spie on 27 Nov 2023
Terms of Use: https://www.spiedigitallibrary.org/terms-of-use

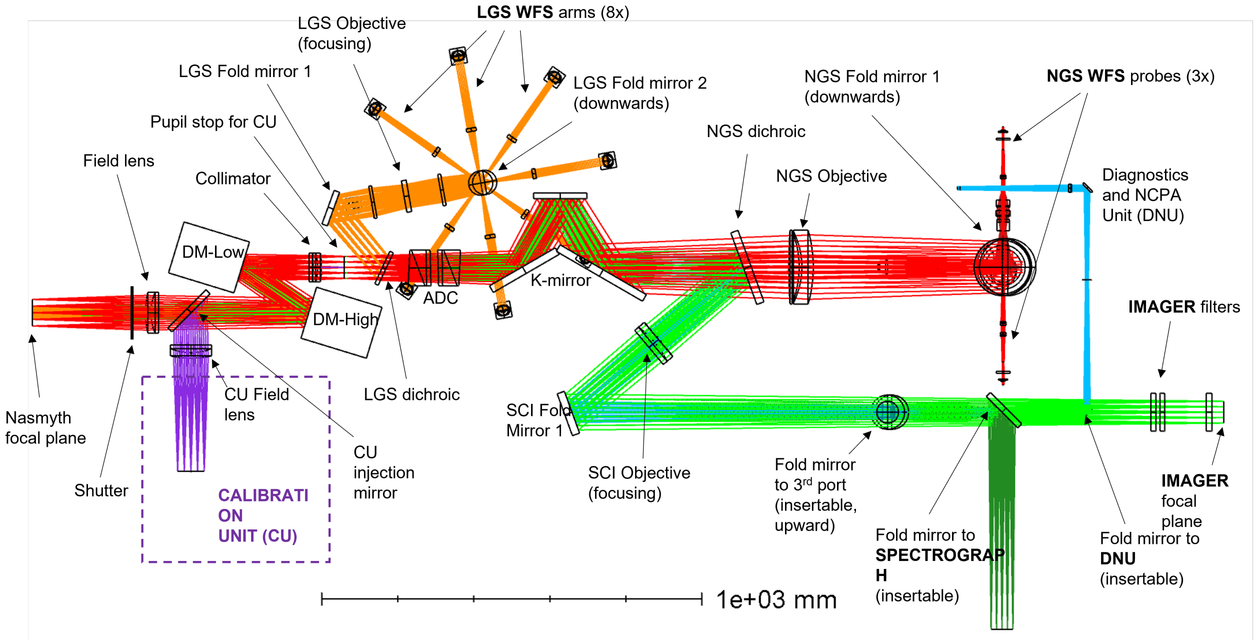

Figure 1. Top view layout. Red rays represent the NGS path, green rays the Science path, orange rays the LGS path, blue rays the DNU path

changing the apparent size of the LGS asterism and providing a constantly telecentric F/8.9 output beam. This allows to have a fixed interface focal plane between the PFR module and the LGS-WFS module, independently from the elevation pointing of the telescope and altitude of the sodium layer used for the generation of LGSs. The two lenses used for the range compensation move together and require only one linear stage for the focus tracking. At the interface focal plane, an eight-faces pyramid mirror reflects each LGS star to one of the WFS arms. The optical layout of one of the LGS-WFS arms is shown in figure 2 (right). The light reflected off the pyramid is collimated by a lens which forms an image of the telescope pupil on a fast steering mirror, used for image jitter compensation. Finally, another couple of lenses are used to relay the image of the pupil on the Shack-Hartmann (SH) lenslet array used for the wavefront sensing. On the intermediate focal plane, placed after the second relay lens, a square field stop is placed to avoid the overlapping between the fields of each lenslet.

In the NGS channel, a three-lens objective forms a telecentric F/20.6 focal plane which serves as optical interface between the PFR and the NGS-WFS. A flat folding mirror sends the light downwards, below the PFR optical bench. The interface focal plane is curved, with a radius of curvature of $463mm$, corresponding to a maximum sag of $\sim 3mm$ at the edge of the FoV. There are three wavefront sensors, shaped as little arms, that can move across the technical field to pick-up the light from NGSs. The NGS-WFS arms are identical but are placed with an offset of 30mm along the focus direction to avoid collisions during movement. Each of them has a field of view of $5.1x5.1arcsec$ and is constituted by a 45° pick-off mirror and a collimator. The collimator is equipped with a motorized focus adjustment which is used to compensate for the field-dependent defocus term generated by the curved focal plane. After the collimator, using a linear stage, it is possible to insert either a single lens or a 2x2 lenslet array. The single lens is used for faint sources and can only measure tip-tilt, the 2x2 lenslet is used for brighter sources and can also measure astigmatism and focus. The camera, an high-speed NIR Saphira detector, is kept at cryogenic temperature and a couple of low-pass filters with $1.4\mu m$ cut-off wavelength are used for the rejection of thermal background.

The part of the field which is not shadowed by the NGS-WFS probes is collected by a field lens and sent to the Acquisition Camera, which provides a feedback for the positioning of the probes in case of failure of the pointing. The Acquisiton Camera re-images the full technical field to a 320x256 detector from Photonic Science with a plate scale of 230 mas/px ($15\mu m$ pixel size).

Downloaded From: https://www.spiedigitallibrary.org/conference-proceedings-of-spie on 27 Nov 2023
Terms of Use: https://www.spiedigitallibrary.org/terms-of-use

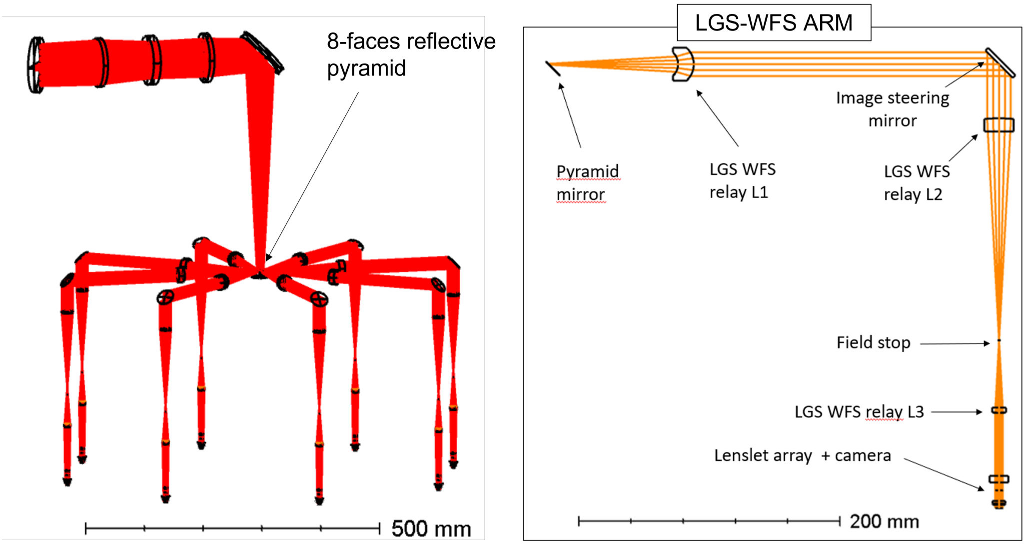

Figure 2. Layout of the LGS-WFS. Left: 3D view with all the 8 WFS arms. Right: 2D view of a single arm.

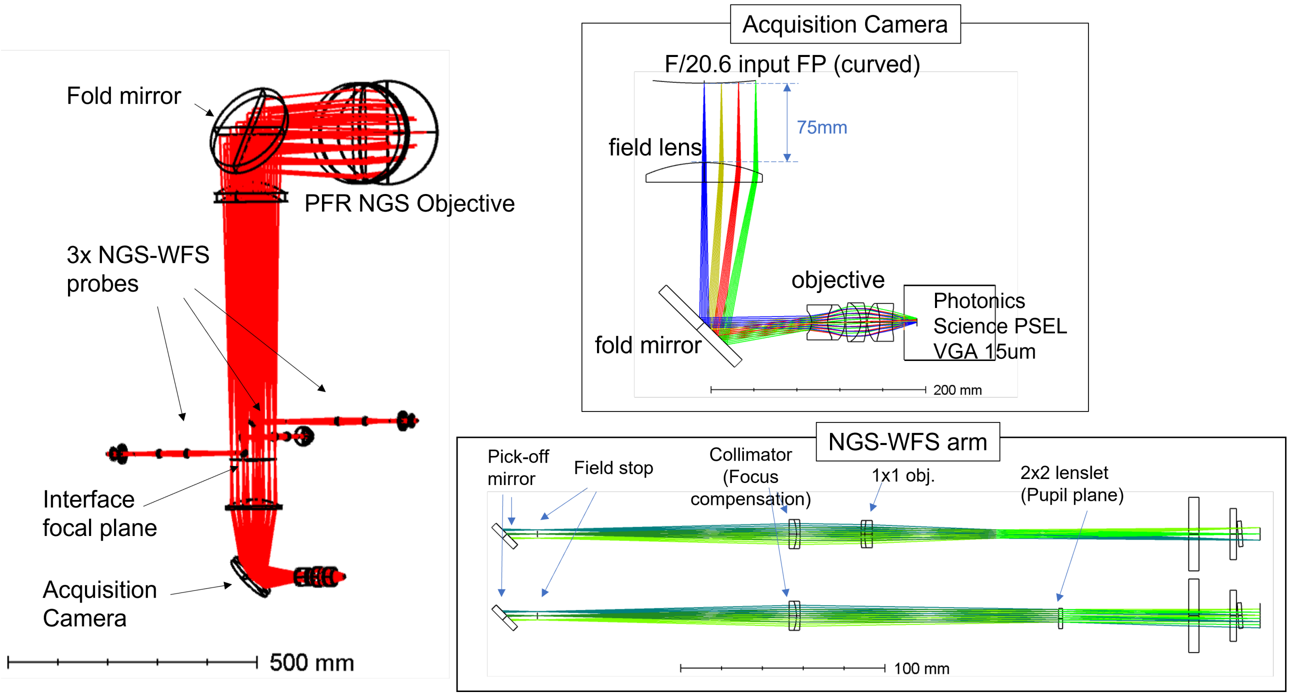

Figure 3. Optical layout of the NGS Channel. Left: 3D view of the complete NGS channel which includes the PFR NGS optics, 3x NGS-WFS probes, and the Acquisition Camera. Right: zoomed 2D view of the Acquisition Camera optics (top) and of one of the NGS arms (bottom) in its 1x1 and 2x2 configurations.

In the Science channel, an achromatic doublet is used to create an F/35 focal plane which serves as optical interface for the instruments. The light can be directed towards three different output ports (see figure 1): 1) straight-through to the Imager, 2) reflected laterally to the Spectrograph by inserting a folding mirror, 3) reflected upwards to the visitor instrument port by inserting a different folding mirror. The doublet can be moved along the optical axis by a motorized linear stage to refocus. The same stage will also be used to retrieve intra ed extra focal images necessary for the calculation of residual non-common path aberrations (NCPAs) with

Downloaded From: https://www.spiedigitallibrary.org/conference-proceedings-of-spie on 27 Nov 2023
Terms of Use: https://www.spiedigitallibrary.org/terms-of-use

the phase diversity technique.

2.1 Optical system parameters

The main optical parameters for each channel and subsystem are reported in the tables below.

Table 1. Optical parameters of the PFR module.

SCIENCE CHANNEL	
Field of view [arcsec]	30×30
Effective focal length [mm]	280000
Aperture ratio	$F/35$
Exit pupil position [mm]	8060
Waveband [nm]	$370 - 1000$

LGS CHANNEL	
Radial field of view [arcsec]	20
Effective focal length [mm]	71000
Aperture ratio	$F/8.9$
Exit pupil position [mm]	infinity
Waveband [nm]	$587 - 591$
Focusing range [km]	$80 - 230$

NGS CHANNEL	
Radial field of view [arcsec]	60
Effective focal length [mm]	164800
Aperture ratio	$F/20.6$
Exit pupil position [mm]	infinity
Waveband [nm]	$1000 - 1740$

MAVIS DEFORMABLE MIRRORS		
	DM-High	**DM-Low**
Conj. distance [km]	13.5	6
Full field footprint [mm]	76.0	68.8
On-axis footprint [mm]	38.1	47.5
Tilt angle [deg]	17	17
On-sky proj. pitch [cm]	31.5	25.3

Table 2. Optical parameters of the NGS-WFS module.

NGS-WFS PROBES		
	2x2 mode	**1x1 mode**
N. sub-aper on pupil diameter	2	1
N. pixel on sub-aperture	128	256
Pixel scale [mas/px]	40	20
FoV diameter [arcsec]	5.1	5.1
Lenslet array pitch [mm]	3.1	6.1

ACQUISITION CAMERA	
Working distance [mm]	75
De-magnification factor	12.5×
Output F/	$F/1.65$
Pixel scale [mas/px]	230
FoV diameter [arcsec]	120

Table 3. Optical parameters of the LGS-WFS module.

LGS-WFS ARMS	
N. sub-aper on pupil diameter	38
N. pixel on sub-aperture	6
Pixel scale [mas/px]	830
Lenslet array pitch [mm]	0.15
Lenslet focal length [mm]	4.4

3. NOMINAL PERFORMANCE

We report here the nominal optical performance at the Science output ports. The image quality is evaluated in terms of RMS WFE. The field of view corrected by MCAO has a diameter of 30 arcsec, while the diagonal of

Downloaded From: https://www.spiedigitallibrary.org/conference-proceedings-of-spie on 27 Nov 2023
Terms of Use: https://www.spiedigitallibrary.org/terms-of-use

the Imager's detector covers a field of 42.4 arcsec. The maximum WFE RMS is 30-35nm in the waveband 850-1000nm. This is due to some residual chromatic defocus and sphero-chromatism which can be partly compensated by refocusing the PSF when observing at a specific passband. At 550nm, the WFE is below 20nm across the full diagonal FoV and below 10nm within the AO-corrected FoV. The design has been also optimized for minimum distortion. The nominal distortion is less than $750\mu as$ within a 15 arcsec radial field. The choice is driven by the fact that, despite distortion can be measured and calibrated, any small variation of the setup could introduce an error on the calibration, which is greater when the system distortion is big.

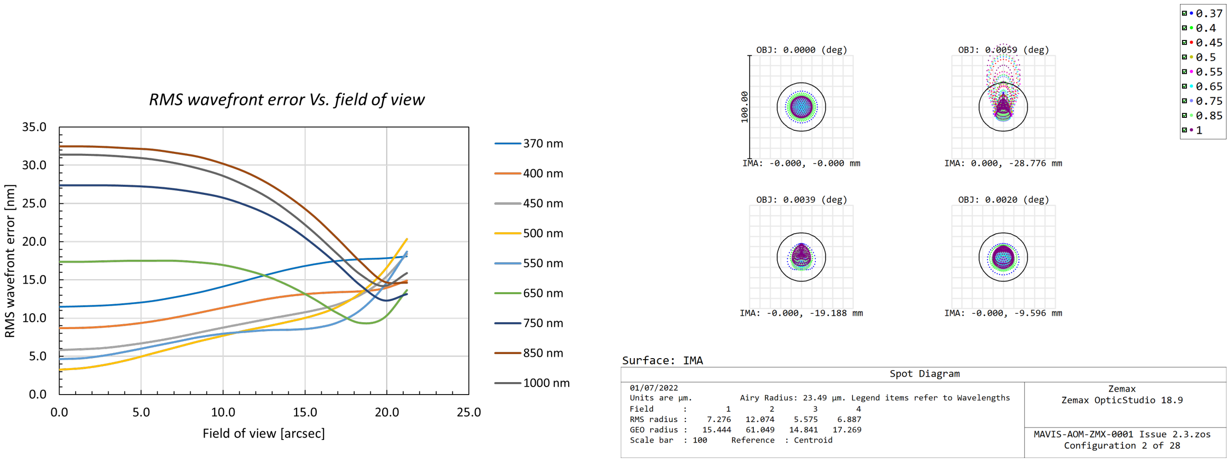

Figure 4. Left: RMS WFE at the science output focal plane as a function of the distance from the optical axis. Different colors denote different wavelengths. Right: Spot diagram at four different field positions.

The compensation of the atmospheric differential refraction is achieved with an ADC composed by two counter-rotating prisms. Each piece is made up of three prisms and the glasses have been chosen to minimize the residual atmospheric dispersion in the full waveband from 370 to 1740nm. The process of optimization is described in Greggio et al.[10] Recently, due to unavailability of thick blanks of the glass N-FK58, the baseline design has changed. The new glass combination (S-FPL55, N-PK51 and PBL1Y) has a PTV residual dispersion of 12 mas at the maximum zenith distance of 65°. Also in the case of the ADC, the residual dispersion can be reduced when observing over a shorter waveband. Figure 5 shows the layout of one of the two identical prisms composing the ADC and the plot of the residual dispersion as a function of wavelength.

4. OPTICAL TOLERANCES

The tolerance analysis has been divided in two parts: one to assess the impact of manufacturing tolerances and the other to estimate the alignment tolerances. Here we present only the results for the Science channel, but the same approach has been used to evaluate the tolerances also of the other channels and modules.

In the manufacturing tolerance analysis, we perturbed the following parameters: radius of curvature, refractive index, Abbe number, wedge, surface figure error (first 55 Zernike polynomials) and center thickness. We started from a sensitivity analysis to identify the worst offenders and we recognized the need of some focus compensators to recover the manufacturing errors on refractive index and radius of curvature of the optical elements. The refocusing is done at two stages: 1) refocusing of the collimator placed after the DMs to collimate the exiting beam, 2) refocusing of the science focal plane by moving the focal plane interface. The second refocusing could have been done by adjusting the position of the science channel achromatic doublet, however, this optical element is already used to generate defocus for the phase diversity measurements and the available movement range is not enough to accommodate also for this compensation. At the moment we are not considering any melt adaptation of the design, but this may added in the future.

After the sensitivity analysis, we adjusted the tolerance values of the worst offenders and we run a Monte Carlo simulation to estimate the probability distribution of the optical performance in the toleranced systems.

Downloaded From: https://www.spiedigitallibrary.org/conference-proceedings-of-spie on 27 Nov 2023
Terms of Use: https://www.spiedigitallibrary.org/terms-of-use

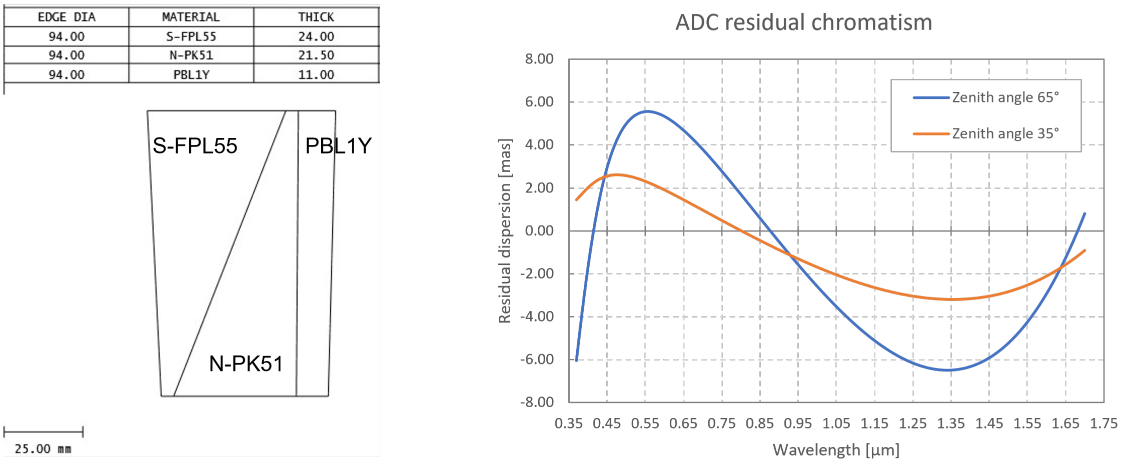

Figure 5. Left: 2D layout of one of the ADC prisms. Right: nominal residual atmospheric dispersion at a zenith distance of 35° (orange curve) and 65° (blue curve).

Figure 6 shows the distribution of the WFE RMS (left) and maximum distortion over the science FoV (right). The 95th percentile value gives an RMS WFE $< 35nm$ and a maximum distortion of 2.4 mas corresponding to about 1/3rd of a pixel in the Imager.

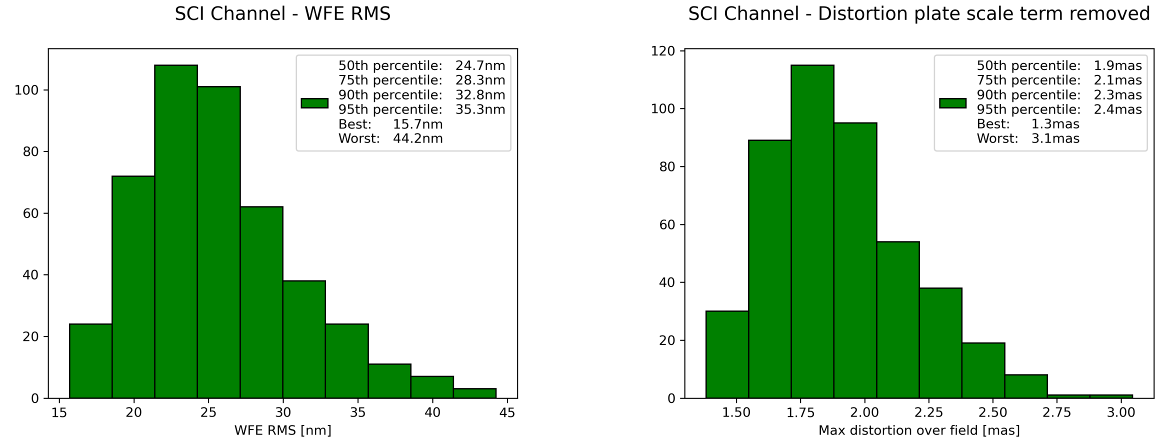

Figure 6. Left: histogram showing the distribution of the RMS WFE (average over FoV and wavelength) obtained from 450 Monte Carlo runs with manufacturing tolerances. Right: histogram of the max distortion over the field of view for the same simulation.

A similar analysis has been conducted for the alignment tolerances. In this case the perturbed parameters were the six degrees of freedom of each optical element. In the case of rotationally-symmetric or flat elements, the rotation around the optical axis was not considered. After a first sensitivity analysis, we setup a customized Monte Carlo simulation reproducing, with a certain level of approximation, the alignment procedure foreseen for the AOM. Optical elements are inserted in the instrument one at a time, starting from flat folding mirrors. The lenses are inserted starting from the last one (Science objective) and each of them is aligned looking at the transmitted and back-reflected spots. An error is added at the end of the procedure to simulate the residuals of the alignment. At the end of the alignment, a final focus adjustment is used to recover the residual defocus. The results are reported in figure 7. The 95th percentile gives a WFE of $18nm$ and a maximum distortion of 1.5 mas, meaning that the alignment is contributing less to the final image deterioration. This is also thanks to the

Downloaded From: https://www.spiedigitallibrary.org/conference-proceedings-of-spie on 27 Nov 2023
Terms of Use: https://www.spiedigitallibrary.org/terms-of-use

fact that, during the design optimization, particular care has been taken to avoid high-power optical surfaces or steep angles of incidence of the rays.

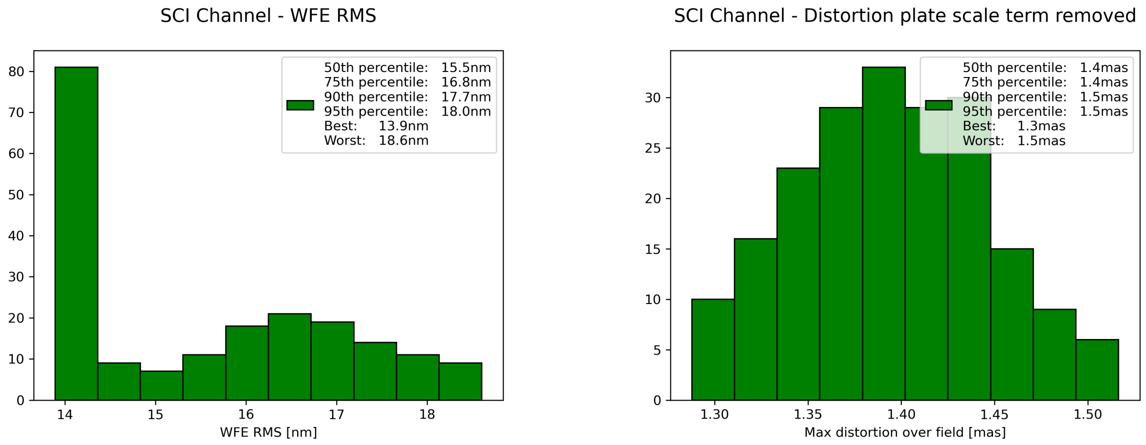

Figure 7. Left: histogram showing the distribution of the RMS WFE (average over FoV and wavelength) obtained from 200 Monte Carlo runs with alignment tolerances. Right: histogram of the max distortion over the field of view for the same simulation.

5. ASTROMETRIC ERROR

It is renown that mid-spatial frequency (MSF) figure errors of optical surfaces could be a dominant term for the astrometric error.[11] This is due to two main reasons:

1. MSF errors on optical elements close to a focal plane contribute to high-order distortion terms which require a lot of sources over the field to be fully characterized.
2. when the footprint of a star moves over an optical surface, like in the common case of field rotation, the distortion experienced by that source may vary more quickly in the case of MSF errors. Also in this case the effect is more pronounced when the optical element is far from a pupil plane.

To assess the impact of the MSF figure error on the relative astrometric error, we ran a set of simulations based on ray-tracing and python. We generated a set of figure error maps starting from a Power Spectral Density distribution of the form:

$$PSD = \frac{A}{f^{\beta}}$$

where f is the spatial frequency in mm^{-1} and we assumed $\beta = 2$ as a typical value for high-quality optics manufacturing.[12] The maps are then normalized to the target RMS surface figure error. As reference, we show in figure 8 an example of figure error map. Using Zemax OpticStudio, we produce a distortion map for a grid of field points covering the scientific FoV. Distortion maps are generated with a script that calculates the centroid for each field point. The centroid calculation is based on ray-tracing. The distortion map is then used as input for the MAVISIM simulation tool.[13] The tool allows to simulate the calibration procedure foreseen for MAVIS,[14] which is based on the measurement of the instrument distortions using a grid of pinholes that is moved in horizontal and vertical directions. The distortion retrieval is based on a first derivative method which reduces the impact of manufacturing errors of the reference grid used for calibration. The output is an estimation of the astrometric error after calibration, due to optics-induced distortion, as a function of separation between field points.

These simulations are aimed at answering two questions:

1. what are the residuals to be expected after calibration in a static scenario

Downloaded From: https://www.spiedigitallibrary.org/conference-proceedings-of-spie on 27 Nov 2023
Terms of Use: https://www.spiedigitallibrary.org/terms-of-use

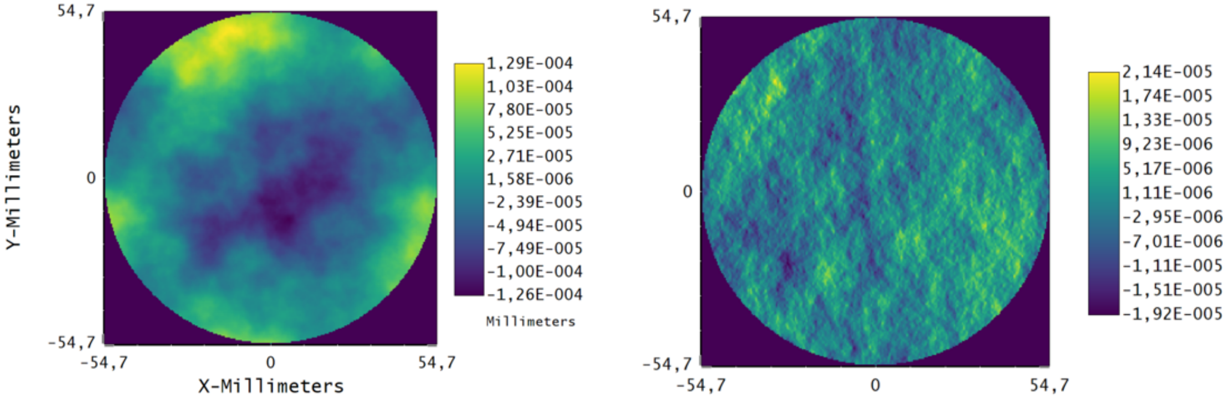

Figure 8. Left: example of a SAG figure error map applied to the field lens with $\beta = 2$, $PTV = 255nm$, $RMS = 50nm$. Right: slope error map in the x direction of the same surface. The RMS slope error is $5\mu rad$.

2. what is the variation of the field distortion due to field rotation (and compensation by the K-mirror)

The static component is produced by all the optics from telescope to scientific focal plane. However, optical elements close to the pupil will have a minor impact on differential distortions over the FoV because the footprints from different sources are almost overlapped and experience the same average deviation. From this point of view, the worst offenders are expected to be the field lens, the SCI fold mirror, the science filters and the cryostat entrance window (the last two being part of the imager sub-system). The distortion variability induced by field rotation, instead, is due to all the optical components in which the beam footprint rotates. The rotation rate is equal to the variation of the parallactic angle for the telescope mirrors and to the combination of parallactic angle and altitude variation for the optical components placed before the K-mirror. In this case the worst offenders are expected to be the field lens and the K-mirror.

To evaluate the static component of the distortion residuals we do the following:

1. We add the MSF error to all the surfaces of one optical element/group.
2. We calculate the centroid position for a grid of 24x24 field points.
3. We calibrate the distortion field with the astrometric calibration package of MAVISIM using a centroiding noise std of $10\mu as$.
4. We evaluate the RMS residuals over the 30 arcsec diameter, after calibration.
5. We evaluate the astrometric error as a function of distance between sources by randomly generating 400 point sources over the FoV and comparing their true distance against the distance reconstructed after calibration.

To evaluate the dynamic component of the distortion residuals generated by field rotation, we simply add the field rotation and compensation in Zemax and calculate a distortion map for every rotation angle. Then we use the distortion map at zero rotation for the calibration of all the other rotation angles.

To assess the sensitivity of different optical elements to the distortion residuals we started by adding MSF figure errors to one group of optical elements at a time. We report here some results obtained for the field lens. The residuals of the calibration of the static distortion map due to the field lens, obtained through MAVISIM using a 11-th order polynomial, are shown on the left side of the figure 9. The RMS residual distortion over the full FoV is $66\mu as$. The plot on the right shows the RMS residuals as a function of the order of the fitted polynomial. For polynomial orders greater than 7 the RMS residual distortion is constant and is dominated by other sources of noise like the centroiding noise. The propagation of centroiding noise through the differential

Downloaded From: https://www.spiedigitallibrary.org/conference-proceedings-of-spie on 27 Nov 2023
Terms of Use: https://www.spiedigitallibrary.org/terms-of-use

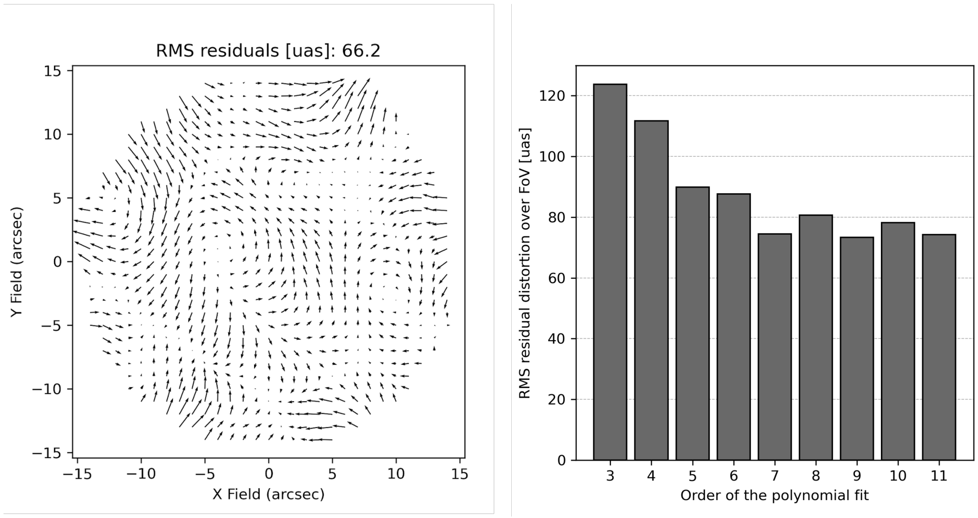

Figure 9. Left: residual distortion map after calibration with a 11-th order polynomial. Right: residual RMS distortion over the full FoV for different orders of the fitting polynomial.

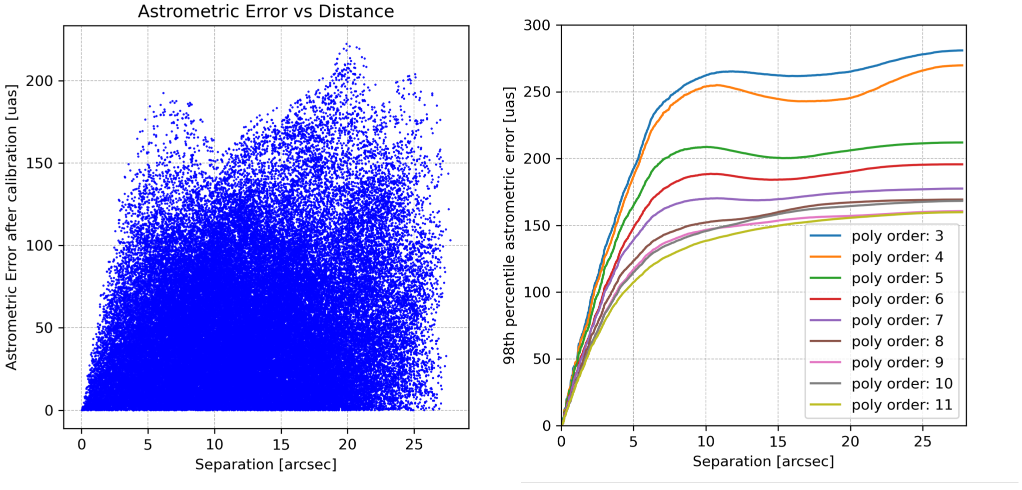

Figure 10. Left: astrometric error after calibration with an 11-th order polynomial fit, for all the star pairs. Right: 98th percentile astrometric error as a function of separation between sources. Colors denote different orders of the polynomial fit.

calibration procedure depends on many parameters: shift of the mask, polynomial order used for fitting and probably also the amplitude and spatial frequency of the distortion to be calibrated.

The plot on the left of figure 10 shows the astrometric error for all the star pairs over the FoV as a function of their nominal distance for the 11-th order polynomial fit. Each point represents a distance measurement between two stars. Starting from this plot, we calculate the "maximum" expected astrometric error as a function of the distance between sources (plot on the right of figure 10). For a certain distance d, the astrometric error is calculated as the 98th percentile of the errors for all the star pairs with distance smaller than d.

For separations of 1 arcsec, the relative astrometric error is less than $50\mu as$; for separations greater than 15 arcsec, the astrometric error can be as good as $150\mu as$ if high-order polynomials are used for the measurement of distortions.

Finally, we report in figure 11 the astrometric error for different field rotations in the case of 1 arcsec (left)

Downloaded From: https://www.spiedigitallibrary.org/conference-proceedings-of-spie on 27 Nov 2023
Terms of Use: https://www.spiedigitallibrary.org/terms-of-use

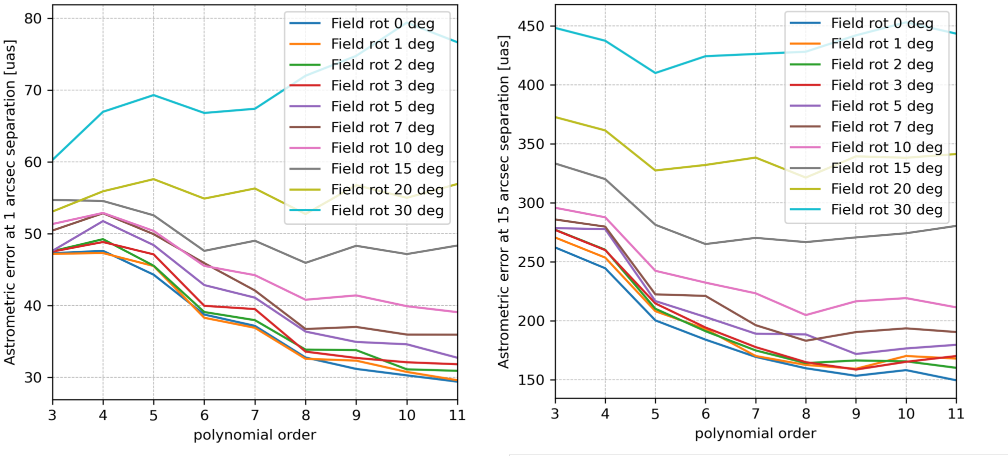

Figure 11. Left: astrometric error (98-th percentile) at 1 arcsec separation as a function of the fitting polynomial order for different field rotations. Right: the same, but with separation of 15 arcsec.

and 15 arcsec (right) separations. As can bee seen from the plot, the distortion calibration is still acceptable for rotations smaller than $\sim 10deg$, and start to de-correlate for higher rotation angles. These results are still preliminary and accounts only for the distortion generated by the field lens. Nonetheless, they give a first assessment of what is the astrometric error contribution that can be expected from optics manufacturing errors. A more complete analysis will be done in the future to validate the results.

Downloaded From: https://www.spiedigitallibrary.org/conference-proceedings-of-spie on 27 Nov 2023
Terms of Use: https://www.spiedigitallibrary.org/terms-of-use

REFERENCES

[1] Rigaut, F., McDermid, R., Cresci, G., Agapito, G., Aliverti, M., Antoniucci, S., Balestra, A., Baruffolo, A., Beltramo-Martin, O., Bergomi, M., Bianco, A., Bonaglia, M., Bono, G., Bouret, J. C., Brodrick, D., Busoni, L., Capasso, G., Carolo, E., Chinellato, S., Colapietro, M., Content, R., Cranney, J., de Silva, G., D'Orsi, S., Ellis, S., Fantinel, D., Fusco, T., Galla, A., Gausachs, G., Gratadour, D., Greggio, D., Gullieuszik, M., Haguenauer, P., Haynes, D., Herrald, N., Horton, A., Kamath, D., Magrini, L., Marasco, A., Marafatto, L., Massari, D., McGregor, H., Mendel, T., Monty, S., Neichel, B., Pinna, E., Plantet, C., Portaluri, E., Robertson, D., Salasnich, B., Savarese, S., Schipani, P., Schwab, C., Smedley, S., Sordo, R., Ströbele, S., Vaccarella, A., Vassallo, D., Viotto, V., Waller, L., Zanutta, A., Zhang, H., Seemann, U., Kuntschner, H., and Arsenault, R., "MAVIS on the VLT: A Powerful, Synergistic ELT Complement in the Visible," *The Messenger* **185**, 7–11 (Dec. 2021).

[2] Ellerbroek, B. L., "Multi-Conjugate Adaptive Optics for Wide Field-of-View Atmospheric Turbulence Compensation," in [*Real Time and Post Facto Solar Image Correction*], Radick, R. R., ed., 15 (Dec. 1993).

[3] Haguenauer, P. et al., "MAVIS: Two for One, the art of LGS multiplication," in [*Adaptive Optics Systems VIII*], Proc. SPIE **12185-283** (2022).

[4] Arsenault, R., Vernet, E., Madec, P. Y., Lizon, J. L., Duhoux, P., Conzelmann, R., Hubin, N., Biasi, R., Andrighettoni, M., Angerer, G., Pescoller, D., Mair, C., Picin, F., Gallieni, D., Lazzarini, P., Anaclerio, E., Mantegazza, M., Fumi, L., Riccardi, A., Briguglio, R., Poutriquet, F., Ruch, E., Rinchet, A., Carré, J. F., and Fappani, D., "Delivery of the Second Generation VLT Secondary Mirror (M2) Unit to ESO," *The Messenger* **151**, 14–19 (Mar. 2013).

[5] Viotto, V. et al., "MAVIS: preliminary design of the adaptive optics module," in [*Adaptive Optics Systems VIII*], Proc. SPIE **12185-72** (2022).

[6] Viotto, V., Agapito, G., Greggio, D., Plantet, C., Pinna, E., Aliverti, M., Arcidiacono, C., Beltramo-Martin, O., Bergomi, M., Bonaglia, M., Busoni, L., Carolo, E., Chinellato, S., Cranney, J., Farinato, J., Fusco, T., Gausachs, G., Gratadour, D., Haguenauer, P., Magrin, D., Marafatto, L., Neichel, B., Radhakrishnan, K., Ströbele, S., Vaccarella, A., Vassallo, D., Esposito, S., Ragazzoni, R., Brodrick, D., and Rigaut, F., "MAVIS: the adaptive optics module feasibility study," in [*Society of Photo-Optical Instrumentation Engineers (SPIE) Conference Series*], *Society of Photo-Optical Instrumentation Engineers (SPIE) Conference Series* **11448**, 114480D (Dec. 2020).

[7] Bonaglia, M. et al., "MAVIS: preliminary design overview of the natural guide star wavefront sensor submodule," in [*Adaptive Optics Systems VIII*], Proc. SPIE **12185-252** (2022).

[8] Ellis, S. C. et al., "MAVIS: imager and spectrograph," in [*Ground-based and Airborne Instrumentation for Astronomy IX*], Proc. SPIE **12184-8** (2022).

[9] Greggio, D., Di Filippo, S., Magrin, D., Schwab, C., Viotto, V., Busoni, L., Esposito, S., Ragazzoni, R., Fusco, T., Benoit, N., Pinna, E., Rigaut, F., Arcidiacono, C., Bergomi, M., Biondi, F., Chinellato, S., Farinato, J., Marafatto, L., Portaluri, E., Radhakrishnan, K., and Vassallo, D., "Optical design trade-off study for the AO module of MAVIS," *arXiv e-prints* **0**, arXiv:2101.11355 (Jan. 2021).

[10] Greggio, D., Schwab, C., Magrin, D., Di Filippo, S., Viotto, V., and Rigaut, F., "Optical design of a broadband atmospheric dispersion corrector for MAVIS," in [*Society of Photo-Optical Instrumentation Engineers (SPIE) Conference Series*], *Society of Photo-Optical Instrumentation Engineers (SPIE) Conference Series* **11447**, 1144755 (Dec. 2020).

[11] Rodeghiero, G., Arcidiacono, C., Pott, J.-U., Perera, S., Pariani, G., Magrin, D., Riechert, H., Glück, M., Gendron, E., Massari, D., Sauter, J., Fabricius, M., Häberle, M., Meßlinger, S., Davies, R., Ciliegi, P., Lombini, M., and Schreiber, L., "Performance and limitations of using ELT and MCAO for 50 μas astrometry," *Journal of Astronomical Telescopes, Instruments, and Systems* **7**, 035005 (July 2021).

[12] Dohlen, K., Wildi, F. P., Puget, P., Mouillet, D., and Beuzit, J.-L., "SPHERE: Confronting in-lab performance with system analysis predictions," in [*Second International Conference on Adaptive Optics for Extremely Large Telescopes. Online at ¡A href="http://ao4elt2.lesia.obspm.fr"¿http://ao4elt2.lesia.obspm.fr¡/A*], 75 (Sept. 2011).

Downloaded From: https://www.spiedigitallibrary.org/conference-proceedings-of-spie on 27 Nov 2023
Terms of Use: https://www.spiedigitallibrary.org/terms-of-use

[13] Monty, S., Rigaut, F., McDermid, R., Baumgardt, H., Cranney, J., Agapito, G., Mendel, J. T., Plantet, C., Greggio, D., Stetson, P. B., Fiorentino, G., and Haynes, D., "Towards realistic modelling of the astrometric capabilities of MCAO systems: detecting an intermediate-mass black hole with MAVIS," MNRAS **507**, 2192–2207 (Oct. 2021).

[14] Cranney, J. et al., "MAVIS: astrometric calibration technique," in [*Adaptive Optics Systems VIII*], Proc. SPIE **12185-235** (2022).

Downloaded From: https://www.spiedigitallibrary.org/conference-proceedings-of-spie on 27 Nov 2023
Terms of Use: https://www.spiedigitallibrary.org/terms-of-use